

The effect of resonance on transient microbubble acoustic response: Experimental observations and numerical simulations

K. Efthymiou, N. Pelekasis, M. B. Butler, D. H. Thomas, and V. Sboros

Citation: *The Journal of the Acoustical Society of America* **143**, 1392 (2018); doi: 10.1121/1.5026021

View online: <https://doi.org/10.1121/1.5026021>

View Table of Contents: <https://asa.scitation.org/toc/jas/143/3>

Published by the [Acoustical Society of America](#)

ARTICLES YOU MAY BE INTERESTED IN

[Numerical analyses of nonlinear behavior of microbubble contrast agents in ultrasound field and effective parameters](#)

The Journal of the Acoustical Society of America **143**, 2111 (2018); <https://doi.org/10.1121/1.5031017>

[Microbubble spectroscopy of ultrasound contrast agents](#)

The Journal of the Acoustical Society of America **121**, 648 (2007); <https://doi.org/10.1121/1.2390673>

[Dependence of the subharmonic signal from contrast agent microbubbles on ambient pressure: A theoretical analysis](#)

The Journal of the Acoustical Society of America **143**, 169 (2018); <https://doi.org/10.1121/1.5020811>

[The fractal derivative wave equation: Application to clinical amplitude/velocity reconstruction imaging](#)

The Journal of the Acoustical Society of America **143**, 1559 (2018); <https://doi.org/10.1121/1.5027237>

[Stability analysis of inverse time domain boundary element method for near-field acoustic holography](#)

The Journal of the Acoustical Society of America **143**, 1308 (2018); <https://doi.org/10.1121/1.5026024>

[Sound scattering and transmission through a circular cylindrical aperture revisited using the radial polynomials](#)

The Journal of the Acoustical Society of America **143**, 1259 (2018); <https://doi.org/10.1121/1.5025159>



CALL FOR PAPERS

JASA
THE JOURNAL OF THE
ACOUSTICAL SOCIETY OF AMERICA

Special Issue:
Lung Ultrasound

The banner features a blue background with a grid pattern and a blurred image of a person's head and neck. A yellow box in the top right corner contains the text 'CALL FOR PAPERS'. The JASA logo is on the left, and the special issue title is in the center.

The effect of resonance on transient microbubble acoustic response: Experimental observations and numerical simulations

K. Efthymiou,¹ N. Pelekasis,^{1,a)} M. B. Butler,² D. H. Thomas,³ and V. Sboros²

¹Department of Mechanical Engineering, University of Thessaly, Volos 38334, Greece

²Department of Physics, Heriot-Watt University, Edinburgh, EH14 4AS, United Kingdom

³University of California, Los Angeles (UCLA) Radiation Oncology, UCLA, Los Angeles, California 90095, USA

(Received 4 September 2017; revised 6 February 2018; accepted 11 February 2018; published online 12 March 2018)

A large number of acoustic signals from single lipid-shelled Definity[®] (Lantheus Medical Imaging, N. Billerica, MA) microbubbles have been measured using a calibrated microacoustic system, and a unique transient characteristic of resonance has been identified in the onset of scatter. Comparison of the numerically obtained response of microbubbles with acoustic measurements provides good agreement for a soft shell that is characterized by small area dilatation modulus and strain softening behavior, and identifies time to maximum radial excursion and scatter as a robust marker of resonance during transient response. As the sound amplitude increases a two-population pattern emerges in the time delay vs the fundamental acoustic scatter plots, consisting of an initial part pertaining to microbubbles with less than resonant rest radii, which corresponds to the weaker second harmonic resonance, and the dominant resonant envelope pertaining to microbubbles with resonant and greater than resonant rest radii, which corresponds to the primary and subharmonic resonances. Consequently, a wider resonant spectrum is observed. It is a result of the strain softening nature of soft lipid shells, based on which the microbubble sizes corresponding to the above resonances decrease as the sound amplitude increases. This bares an impact on the selection of an optimal microbubble size pertaining to subharmonic imaging. © 2018 Acoustical Society of America.

<https://doi.org/10.1121/1.5026021>

[GH]

Pages: 1392–1406

I. INTRODUCTION

The introduction of viscoelastic shells to physically stabilize microbubbles over prolonged periods *in vivo* (Feinstein *et al.*, 1990) has enabled their safe and reproducible usage as contrast agents in diagnostic ultrasound, providing locally increased echogenicity while improving the sensitivity and specificity of diagnostic imaging. By enhancing the contrast at the tissue–blood interface, information on the dynamics of the vascular bed can be provided (Ferrara *et al.*, 2007; Kaufmann *et al.*, 2007). However, qualitative measurements are limited for diagnostic evaluation and the primary aim of contrast enhanced ultrasound (CEUS) has been to assess microvascular flow and volume quantitatively (Strouthos *et al.*, 2010). The knowledge of the interaction of microbubbles with ultrasound has advanced considerably (Sboros, 2008). In addition, new ultrasound techniques that aim to increase spatial resolution by tracking the echoes of single microbubbles have been developed (Christensen *et al.*, 2015; Errico *et al.*, 2015). The understanding of the evolution of a microbubble echo during an exposure to ultrasound becomes more important. The unique and largely unexplored effect of the protective coating, especially for the case of lipid shells (Overvelde *et al.*, 2010; Tsigliferis and Pelekasis, 2013) that are used commonly, provides the potential for significant improvement in contrast-to-tissue

ratio and identification of an individual microbubble signature that enables robust tracking.

Here we deal with a particular oscillatory signature associated with resonance and that can be unique to a microbubble. This behavior is fundamental in the understanding of the dynamics of contrast bubbles that has been under-investigated. Previous studies have characterized microbubble response by studying the acoustic emissions and absorption characteristics from high concentrations of microbubbles, deducing the overall resonance behavior of the sample (Frinking and de Jong, 1998; Shi and Forsberg, 2000). Such approaches provided microbubble population measurements and are thus limited in providing individual microbubble signatures. More recently, a large number of publications have studied the oscillations of microbubbles in the presence of ultrasound fields by employing ultrahigh speed optical imaging to capture the radial oscillations with time (Bouakaz *et al.*, 2005; Chin *et al.*, 2003; Dayton *et al.*, 1999), which has uncovered examples of previously unseen microbubble behavior (Postema *et al.*, 2003; Emmer *et al.*, 2007; de Jong *et al.*, 2007). A common thread in most of these pioneering studies was the short pulse duration that did not reveal acoustic response patterns during ultrasound exposure. The variations of microbubble size and shell parameters within a typical sample of contrast agents (Postema *et al.*, 2003) dictate that a large number of single scatter data are necessary to obtain information on the variability of microbubble response. In particular, optical techniques employed for capturing the

^{a)}Electronic mail: pel@uth.gr

time evolution of bubble radius during small amplitude oscillations reveal the resonant pattern of coated microbubbles and provide estimates of the shell elasticity and viscosity (van der Meer *et al.*, 2007). Furthermore, optical studies (Emmer *et al.*, 2007; de Jong *et al.*, 2007; Dayton *et al.*, 1999; Morgan *et al.*, 2000) establish that microbubbles are resonant bodies that pulsate in a nonlinear fashion in response to ultrasound, and attempts to explain the physical origin of these have been made (Marmottant *et al.*, 2005; Tsigliferis and Pelekasis, 2008; Overvelde *et al.*, 2010).

In order to deduce useful conclusions on the physical behavior of bubbles, the majority of the available studies concentrate commonly on the steady state of oscillating response, which is well after the initial response. The transient response arising from the natural resonance frequency is therefore nearly always ignored and the related literature is then sparse. However, for very short pulse durations even at low pressure amplitudes transient effects are manifested in the acoustic response. The importance of identifying resonance conditions from transient data has been previously investigated in the context of free bubbles (Flynn and Church, 1988), where it was seen that imposition of an ultrasonic wave of a certain large amplitude (5 Atm) facilitates the onset of transient cavitation of smaller and smaller bubbles as the sound frequency increases. Using the Rayleigh–Plesset model, Leighton (1989) presented results on the oscillations of free bubbles, which included initial transient oscillations. He thus showed that before the oscillations settle to the steady state response, the short-lived transients can enhance the amplitude of oscillations, in some cases leading to unstable cavitation or the collapse of smaller bubbles.

Similar effects, associated with the impact of the phase of the pulse on the acoustic response, are discussed by Morgan *et al.* (2000). They have used a modified Herring equation with parameters fitted to optically observed oscillations of an experimental lipid shelled contrast agent, MP1950 (Mallinckrodt, Inc., St. Louis, MO), to distinguish that transient effects may appear on the first few cycles of response at relatively low acoustic pressures (~ 100 kPa). By comparing single cycle transmit pulses starting with either compression or rarefaction (i.e., 180° out of phase), they predict that the initial cycles of bubble oscillation are initiated by the driving rarefaction in either case, causing a lower mean frequency echo from transmission of compression first. The transient response, which is dependent on both bubble size relative to resonance and individual shell parameters, gradually damps out as the duration of the driving pulse increases.

Acoustic studies of single microbubbles have also been performed (Sboros *et al.*, 2003), enabling the absolute measurement of scatter (Thomas *et al.*, 2009a; Sijl *et al.*, 2008). In comparison to optical data (Sijl *et al.*, 2011) that measure radial oscillations, the acoustic experiments measure the scattered pressure field, which is a consequence of shell velocity and acceleration (de Jong *et al.*, 1994b; Church, 1995; Goertz *et al.*, 2007; Thomas, 2009b). Acoustical studies thus offer information directly relevant to the application of microbubbles in imaging by enabling echo processing investigations (Thomas *et al.*, 2009a). However, although of high relevance to imaging, it remains unclear whether microbubbles resonate

or not *in vivo*. The reference to resonating microbubbles is very common in the literature, but current signal processing, which includes pulse sequences such as pulse inversion and amplitude modulation, exploits only the fact that microbubbles behave nonlinearly without distinguishing between resonance and off resonance. However, it is now known that resonant microbubbles provide a transient acoustic response of growing amplitude (Thomas *et al.*, 2009b). This work is further investigated here aiming to further our understanding of the relationship between resonance and transient acoustic response, which may be controlled by employing the nonlinear nature of the microbubble shell constitutive law, especially at large sound amplitudes.

Theoretical modeling of the oscillations of microbubbles has been the subject of many studies. Several models based on the Rayleigh–Plesset equation have been developed to account for various aspects of the encapsulating shell behavior. de Jong *et al.* (1994a,b) and Church (1995) have extended the Rayleigh–Plesset model further by including extra terms for shell damping, relating shell elasticity and viscosity parameters to experimental data from attenuation and backscattering measurements. More recently, the Kelvin–Voigt model has been used to model the shell mechanical behavior, coupled with the Keller–Miksis model (Keller and Miksis, 1980) for the bubble acoustic response, to derive expressions of resonance frequency and damping coefficients, and to account for nonlinearity in the shell response as a result of large amplitude sonication and departure of the shell constitutive law from linearity (Tsigliferis and Pelekasis, 2008). Numerical solution of these various models, which has been used for a comparison to the data from high speed optical experiments, allows for calculation of the bubble radius as a function of time. An important criticism for such a comparison comes from the fact that the majority of optical experiments are done next to a boundary, e.g., the capillary wall, which is often not taken into consideration in these comparisons. As the capillary wall adds to the complexity of the flow arrangement, microbubbles pulsating at a distance from boundaries, such as those that are obtained via manipulation with optical tweezers (Dollet *et al.*, 2008), provide experimental data that are optimal for such comparisons. However, these experiments are difficult to make and thus sparse in the literature. The microbubble scatter pressure can be viewed as an alternative or a complementary physical quantity that can provide a comparison between theory and experiment. The theoretical scattered pressure can be calculated by using the Bernoulli equation to relate pressure to the velocity/acceleration of the bubble wall. In this way, theoretical models of microbubble behavior can be directly compared to both acoustic and optical experimental measurements, allowing significant additional physical insight on the behavior of the shell. It should be stressed, however, that in the present study nonspherical effects are not accounted for in the analysis that is presented, and therefore special care is taken in our experiments to avoid jetting or breakup phenomena, such as those that occur during acoustic measurements when microbubbles pulsate next to a rigid boundary at large amplitudes.

Presented here is a combined experimental and theoretical investigation into the single pulse response of the contrast agent Definity[®] (Lantheus Medical Imaging, N. Billerica, MA). The aim of this paper is to study the effect of resonance on the transient response of a lipid contrast agent with a disperse size distribution with emphasis placed on the effect of increasing sound amplitude. Previous literature suggests that transient response in the emissions from short diagnostic pulses, such as the ones investigated here both experimentally and theoretically, may provide significant information (Leighton, 1989; Morgan *et al.*, 2000; Thomas *et al.*, 2009b; Raymond *et al.*, 2015). More importantly, the comparison of transient response in the theoretical and experimental data may provide a significant test for the constitutive law, an important implication that is also discussed herein. Careful analysis of the acoustic data obtained in the present study reveals that resonant behavior can be captured even from relatively short range pulses by utilizing the rich harmonic content of the backscattered pressure signal from soft phospholipid shells, as well as the time required for resonant response to take place between the forcing and the natural frequency of the microbubble.

II. METHODS

A. Theory of microbubble response

1. Basic formulation and numerical methodology

The effect of the transient response on resonant scatter is investigated here using the Keller–Miksis (Keller and Miksis, 1980) model that accounts for a moderately compressible surrounding fluid (see also Prosperetti and Lezzi, 1986), adapted by Tsiglifs and Pelekasis (2008) for the forced oscillations of encapsulated bubbles by incorporating various constitutive laws pertaining to the mechanical behavior of the shell. The incident pressure waves as measured experimentally using a membrane hydrophone were used as the driving force in the model. The soft phospholipid shell of Definity[®] (Lantheus Medical Imaging, N. Billerica, MA) is treated as a strain-softening material in the manner defined by the Mooney–Rivlin (MR) constitutive law, as originally proposed by Tsiglifs and Pelekasis (2008, 2011, 2013); see Eqs. (3a) and (3b) below for spherically symmetric pulsations of a coated microbubble, and verified later via systematic acoustic measurements (Thomas *et al.*, 2009b) and independent simulations (Paul *et al.*, 2010).

When the wavelength of the acoustic wave is much larger than the bubble radius the far field pressure and radial position of the coating assume the form

$$R = 1 + \varepsilon R_d, \quad P_\infty = P_{st} + \varepsilon P_{st} \sin(\omega_f t), \quad (1)$$

with P_{st} and ε denoting the static pressure and amplitude of the external forcing, respectively, R, R_d are the dimensionless instantaneous radial position and its deviation from the stress free radius R_0 taken as the characteristic length, respectively, and ω_f is the forcing frequency. The nonlinear ordinary differential equation (ODE) that describes the acoustic response of a radially pulsating microbubble has been solved numerically

for a variety of bubble radii and acoustic disturbances using the numerical methodology developed previously (Tsiglifs and Pelekasis, 2008). The latter entails employment of the Runge–Kutta time integrator coupled with the adiabatic law of ideal gases for the evolution of the radial position and internal pressure. The scattered pressure P_{sc} at a distance $r = 0.075$ m for a given microbubble radius R_0 was calculated in order to match the measured values. Once microbubble scattered acoustic signals were calculated, similar analysis as performed on the experimental signals was performed in terms of the Fourier spectrum and root-mean-square (RMS) of the scattered pressure and the extraction of 95% response time, $\Delta t_{95\%}$, in order to allow comparison; $\Delta t_{95\%}$ signifies the time required to achieve 95% of maximum scattered pressure.

The shell parameters of the model and the incident pulse duration were varied in order to investigate the effect of transient response on longer pulses, up to 30 cycles, as well as the possibility for the onset of steady pulsations. The experimental setup did not allow pulses of this duration to be measured as the pulse length was limited by the maximum separation between microbubbles that the flow tank would allow for a reasonable sampling-time interval to be established. However, numerical analysis allows for the investigation of a wider parameter range, thus, providing further insight on the short pulse experimental results in contrast to those pertaining to steady pulsation. This long duration enables steady pulsation to be established and an investigation on the relation between transient response and constitutive law to be carried out.

The main parameters used to describe the behavior of the encapsulating lipid shell are the area dilatation modulus $\chi_s = 3d_s G_s$, with d_s and G_s denoting shell thickness and stiffness, respectively, and shell viscosity μ_s (Hoff *et al.*, 1996). The values for these are initially chosen as $\mu_s = 1$ Pa s and $\chi_s = \chi = 2.25$ N/m, corresponding to effective shell thickness and stiffness on the order of $d_s = 15$ nm and $G_s = 50$ MPa, respectively (Goertz *et al.*, 2007; Cheung *et al.*, 2005). It should also be stressed that, due to the nature of phospholipid shells, their shell thickness cannot be easily defined hence the area dilatation modulus, χ , along with bending resistance, k_b , are considered as the primary shell mechanical properties. These values have been shown previously to provide a reliable fit on the scatter from a distribution of Definity[®] (Lantheus Medical Imaging, N. Billerica, MA) microbubbles, in the form of scattering cross-section and resonance frequencies (Tsiglifs and Pelekasis, 2008; Thomas *et al.*, 2009b; Tsiglifs and Pelekasis, 2011);

$$\omega_0 \approx \sqrt{(3\gamma - 1) \frac{2\sigma}{\rho_\ell R_0^3} + \frac{3\gamma P_\infty}{\rho_\ell R_0^2} + \frac{4\chi}{\rho_\ell R_0^3}}. \quad (2)$$

Primary resonance frequency (ω_{res}) and the associated primary resonance radius (R_{res}) is defined as the frequency at which fundamental scatter is at a maximum (Church, 1995; Khismatullin and Nadim, 2002; Tsiglifs and Pelekasis, 2008). In this fashion, the radial position of the microbubble interface with the surrounding medium is obtained by

solving a nonlinear ODE that incorporates the effects of shell elasticity and viscosity along with inertia, compressibility, and viscous effects from the surrounding medium. The model equations for a strain softening shell without prestress are reproduced below for completeness, as introduced by Tsiglifis and Pelekasis (2008),

$$\begin{aligned} (1 - MR')R'\ddot{R}' + \left(\frac{3}{2} - \frac{MR'}{2}\right)\dot{R}'^2 \\ = (1 + MR')\left(P'|_{r=R} - P'_{st} - P'_{Ac}\right) \\ + MR' \frac{d}{dt'} \left(P'|_{r=R} - P'_{Ac}\right), \end{aligned} \quad (3a)$$

$$\begin{aligned} P'|_{r=R'} = \left[\frac{2}{We} + P'_{st}\right] \left(\frac{1}{R'}\right)^{3\gamma} - \frac{2}{WeR'} - \frac{4}{Re_j R'} \\ - \frac{4m}{Re_j R'^2} - 2\frac{G}{R'} \left(1 - \frac{1}{R'^6}\right), \quad t' = \omega_f t, \\ R' = \frac{R}{R_0}, \end{aligned} \quad (3b)$$

$$\begin{aligned} P' = \frac{P}{\rho\omega_f^2 R_0^2}, \quad G = \frac{\chi_s}{3\rho_l\omega_f^2 R_0^3}, \quad m = \frac{3\mu_s}{\mu_l R_0}, \\ Re_j = \frac{\rho_l\omega_f R_0^2}{\mu_l}, \quad We = \frac{\rho_l\omega_f^2 R_0^3}{\sigma}, \quad M = \frac{R_0\omega_f}{c}; \end{aligned} \quad (3c)$$

in the above relations primes signify dimensionless quantities defined via the initial bubble radius R_0 and forcing frequency ω_f , and M denotes the Mach number taken to be small.

In order to obtain a reliable estimate of shell thickness of lipid shells we have also carried out a parametric study in the area dilatation modulus χ_s , and investigated the impact on the acoustic response of both MR and Hooke's law.

2. Theoretical basis of the transient response

Figure 1 shows examples of the radial time series for coated microbubbles below, at and above resonance, in response to a 6 cycle [Figs. 1(a)–1(c)] and 20 cycle [Figs. 1(d)–1(f)] acoustic disturbance. The former case simulates a situation where transient response is still dominant, whereas in the latter the onset of steady pulsations is evident toward the end of the pulse. Nevertheless, the aspects of resonant response are evident in both cases. In particular, the bubble acoustic response occurs as a superposition of two oscillations: (1) the steady state oscillation at the driving frequency ω_f , and (2) a damped natural oscillation at the natural frequency of the resonator ω_0 , which is subject to an approximately exponential decay, ω_R governed by the damping characteristics of the system. If the two responses are in phase, as occurs when a microbubble is driven approximately at resonance [Figs. 1(b) and 1(e)] energy transfer between the two modes of oscillation takes place. Consequently, the amplitude of the radial time series is modulated and grows over time during the phase of transient pulsation, eventually settling to the steady state response as the transient damps out (Flynn and Church, 1988). This will generate an envelope of response in experimental and theoretical data near resonance

before steady pulsation is achieved, and it is the expression of the delay of the onset of maximum response. Figures 1(g)–1(i) and 1(j)–1(l) depict the amplitude of the major Fourier components in dB pertaining to the RMS scattered pressure at a distance of 7.5 cm from the microbubble center over the duration of a 6 and 20 cycle pulse, respectively,

$$p_{Sc} = p - p_\infty \approx -\rho \frac{\partial\phi}{\partial t} = \frac{\rho R}{d} (R\ddot{R} + 2\dot{R}^2), \quad (4a)$$

$$\begin{aligned} p_{Sc}(t) = \sum_{n=-\infty}^{\infty} c_n e^{-i(2n\pi/\Delta T)t} \rightarrow p_{Sc,RMS} \\ = \sqrt{c_0^2 + \sum_{n=1}^{\infty} \frac{|c_n|^2}{2}}, \end{aligned} \quad (4b)$$

$$P_{n,Amp} = 20 \text{ Log} \left(\frac{\sqrt{\frac{|c_n|^2}{2}}}{p_{Ref}} \right), \quad p_{Ref} = 1 \text{ atm.} \quad (4c)$$

Corrections to the scattered pressure due to compressibility effects are dropped as they are order M^2 (Keller and Miksis, 1980), with $M = (R_0\omega_f)/c$ denoting the Mach number of the flow and $c \approx 1500$ m/s is the speed of sound in the liquid. Primary resonance is dominated by the fundamental component and this is illustrated by the fast Fourier transform (FFT) decompositions shown in Figs. 1(h) and 1(k), corresponding to the RMS scattered pressure calculated for the radial time series shown in Figs. 1(b) and 1(e). The latter graphs clearly illustrate the resonant envelope and the accompanying growth of the radial position.

If the frequencies ω_f and ω_0 are sufficiently different then, depending on whether the bubble is insonated below or above resonance, two different types of response are registered. For bubbles whose sizes are below resonance, i.e., ω_0 is larger than ω_f , viscous damping is larger and steady pulsations are achieved quickly (i.e., the insonating pulse is of identical shape to the scattered one) as illustrated in Figs. 1(a) and 1(d). In this case the fundamental and second harmonic components of the FFT spectrum are of the same order, as shown in Figs. 1(g) and 1(j). Furthermore, due to their larger resonance frequency such relatively small bubbles tend to participate in second harmonic resonance, $2\omega_f$, as the sound amplitude increases. For relatively large bubbles damping is relatively weak, and both modes of pulsation are evident for a longer time period with the maximum occurring at an earlier stage of the pulsation [Figs. 1(c) and 1(f)]. It should also be noted that for such large bubbles, whose resonant frequency is smaller, the possibility of subharmonic resonance is also present, and this is manifested in the gradual onset of the subharmonic component, $\omega_f/2$, in the FFT spectra shown in Figs. 1(h) and 1(k). The latter effect will be seen in the following to be more pronounced especially for large sound amplitudes. In fact, nonlinearity is known to decrease or increase the resonance frequency depending on the nature of the oscillator while introducing additional modes of pulsation in the dynamic response. In this context, Church (1995) refined the Rayleigh–Plesset model for the albumin shelled agent

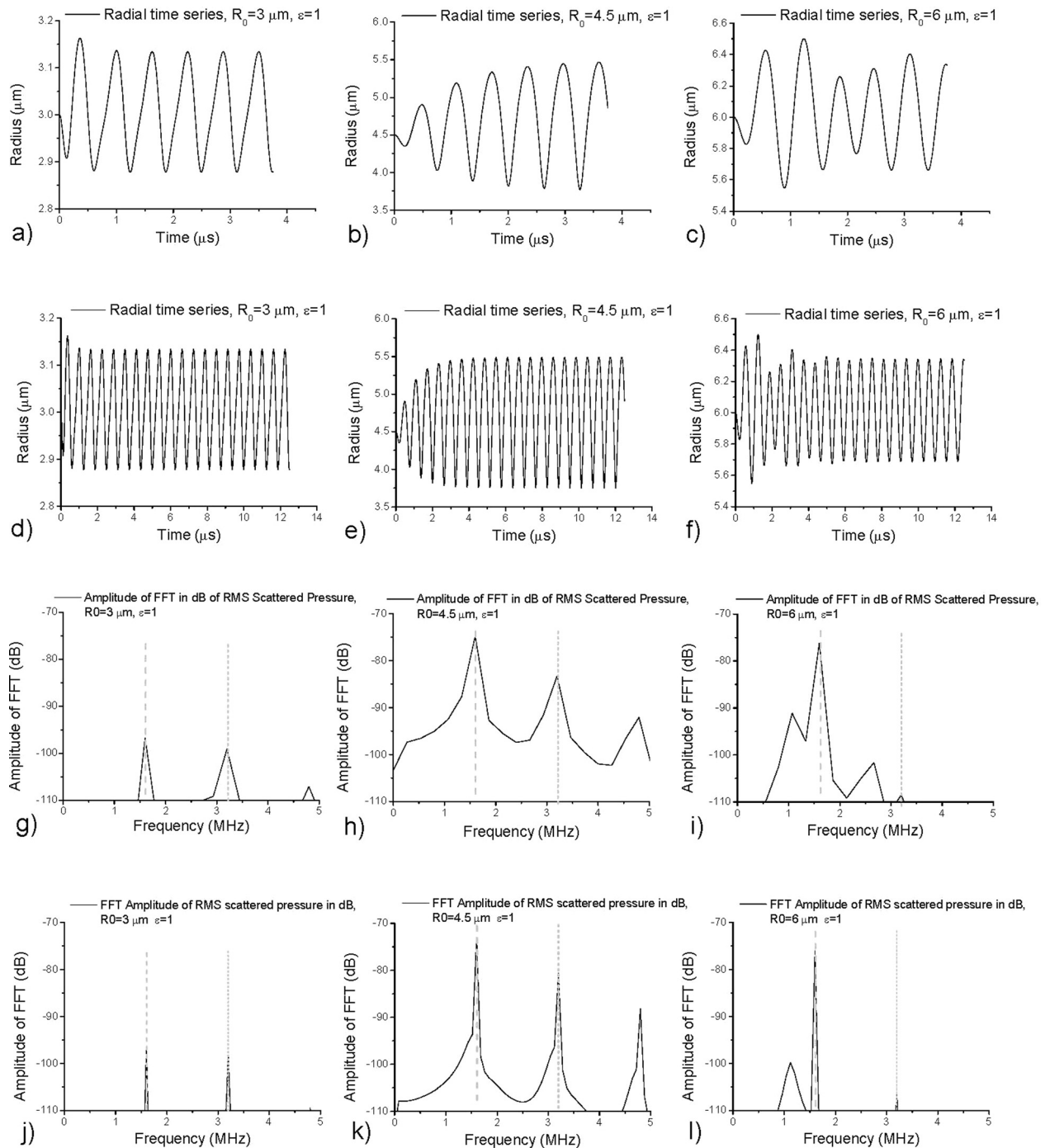


FIG. 1. Numerically obtained radial time series in response to a sinusoidal disturbance of rectangular shape with frequency 1.6 MHz and amplitude 100 kPa that lasts over 6 cycles, graphs (a)–(c), and over 20 cycles until steady pulsation has been achieved, graphs (d)–(f). The MR shell model is employed (Tsigliris and Pelekasis, 2008) with shell parameters $\chi_s = 2.25 \text{ N/m}$ and $\mu_s = 1 \text{ Pa s}$. Graphs (g)–(i) and (j)–(l) provide the fast Fourier transform (FFT) decomposition of the root-mean-square (RMS) scattered pressure, calculated via Eq. (4) for the cases shown in (a)–(c) and (d)–(f), respectively.

Albunex[®] (Molecular Biosystems, San Diego, CA), and obtained a weakly nonlinear analytical solution for the nonlinear ODE describing the bubble oscillation. He focused on the part of the microbubble response where the pulsation is steady and captured the onset of harmonics during the periodic bubble pulsation as a function of the acoustic pressure amplitude.

B. Experimental methodology

The experimental method has been previously detailed in Sboros *et al.* (2005). Briefly, acoustic signals from single

Definity[®] (Lantheus Medical Imaging, N. Billerica, MA) phospholipid shelled coated microbubbles containing an octafluoropropane (C_3F_8) gas have been measured experimentally using a modified commercial ultrasound imaging system (Sonos5500, Philips Medical Corp, Andover, MA) with a fully characterized transmitter and receiver, allowing calibrated radio frequency (RF) signals to be obtained. The incident acoustic field was measured using a 0.2 mm active element membrane hydrophone (Precision Acoustics Ltd., Dorchester, UK). The transmit frequency was set at

1.6 MHz, and the acoustic pressure ranged from 187 to 550 kPa peak negative pressure. Optical studies show a fragmentation threshold around 300 kPa (Chomas *et al.*, 2001), but this is obtained under the optical experiment conditions where the microbubbles are in contact with the tube wall. An extensive comparative review suggests that in free space the fragmentation threshold is at much higher acoustic pressures and correlates with microbubble disruption (Stride and Saffari, 2003; Sboros, 2008). This is supported by data for Definity[®] (Lantheus Medical Imaging, N. Billerica, MA) microbubbles that show that below 500 kPa nearly all microbubbles survive (Sboros *et al.*, 2007). Thus, the adopted acoustic pressure range here provides very little destruction, which only occurs for quite large rest radii ($R_0 \geq 5 \mu\text{m}$). For this reason we rejected microbubble echoes that do not provide similar amplitude in response to the second insonation. RF scatter data sampled at 20 MHz were recorded at a distance of 1 cm between 7 and 8 cm from the face of the transducer. The backscattered RF data were calibrated using individual copper spheres (Sboros *et al.*, 2005). Low concentrations of contrast agent were injected into a flow tank, allowing a submillimeter-wide stream of single microbubbles to be directed along the axis of the ultrasonic beam as previously (Sboros *et al.*, 2007; Thomas *et al.*, 2009b). This ensures that each microbubble will be in the center of the ultrasound path, and will be insonated by the same acoustic pressure (Sboros *et al.*, 2007; Thomas *et al.*, 2009b). A suitable concentration of microbubbles (1 in 10 000 by volume) and a low pulse repetition frequency (i.e., one imaging pulse every 2 s) gave an average of one microbubble in the 1 cm axial region of interest every three imaging pulses, thus, ensuring a very low probability of having two microbubbles within a scattered pulse of identical duration to the transmit. Data were collected in batches of three repeat measurements at each set of incident parameters. The pulse length was set at six cycles, which is a sufficiently long pulse to observe the transient response. The choice of longer pulses is desirable but rather problematic under the current experimental setup: (a) a longer region of interest would need to be chosen (longer than 1 cm), which would subject microbubbles to wider range of acoustic pressures and (b) there is a higher probability of overlapping scatter signals, which may affect the quality of the data. Custom software allowed individual lines of RF echo to be captured and converted to text files for further analysis in MATLAB (R2007b, MathWorks, MA). A sum-squares technique was used to identify microbubble signals that are above noise, and a semi-automatic edge detection method used to define the start and end of each microbubble signal. Once individual microbubble RF signals were extracted, the duration of the transient component of response was identified by calculating the time taken from the onset of scatter to reach 95% of the maximum amplitude obtained in each signal ($\Delta t_{95\%}$). RF signals were corrected for offset and decomposed into their fundamental and harmonic signals, using a fourth-order elliptical filter with a passband of 800 kHz centered at the respective frequencies. This allowed the individual components of harmonics to be calibrated in an absolute manner (Sboros *et al.*, 2005) and thus compared with theoretical scatter. From these calibrated signals, RMS fundamental and second harmonic pressures were

calculated, and results presented here are given in values of Pascals (Pa); capturing the subharmonic component of the acoustic response was beyond the capabilities of the receiver, hence, it is not shown in the experimental results that follow (Sec. III). Signals have been classified as resonant or nonresonant using a cluster method depending on fundamental dominance of scatter (Thomas *et al.*, 2009b), and they are analysed with respect to their duration of transient response ($\Delta t_{95\%}$).

III. RESULTS AND DISCUSSION

A. Experiment

Signals from both resonant and nonresonant microbubbles were detected in response to a six-pulse cycle with a frequency of 1.6 MHz and a peak negative pressure of 550 kPa, with a marked difference in the amplitude and envelope shape between the two. Figure 2 shows RF signals, frequency spectra, and fundamental filtered signals from four example bubbles: two microbubbles below resonance and two microbubbles at or above resonance. The microbubble signals shown in Fig. 2 are measured in response to the same incident pulse parameters, and show typical behavior of either off-resonance [Figs. 2(a) and 2(b)] or resonance scatter [Figs. 2(c) and 2(d)]. Resonant bubbles are characterized by increased amounts of fundamental scatter, as shown in Fig. 2(e), which is a scatter-plot showing the fundamental and second harmonic components of RMS scattered pressure in each case of 235 single acoustic microbubble signals. Twenty-six microbubble signals have been classified as resonant using a cluster method dependent on fundamental dominance of scatter (Thomas *et al.*, 2009b). These primary resonant scatterers account for 11% of the total bubble signals measured, and produce the majority of the total fundamental energy of scatter: 70% of the fundamental, 15% of the second harmonic.

The six cycle RF signals show the effect of resonance on both frequency content and envelope of response. Bubbles below resonant size [Figs. 2(a) and 2(b)] emit strongly harmonic signals with fundamental to harmonic ratio of order 1. They have an approximately rectangular envelope of response, similar to the transmit pulse. Here we use time taken to reach a value of 95% of peak scatter ($\Delta t_{95\%}$) as a measure for the duration of the transient response. In response to 550 kPa, nonresonant bubbles, i.e., RMS fundamental scatter less than 8 Pa, all have $\Delta t_{95\%} < 2.5 \mu\text{s}$ with a mean value $\overline{\Delta t_{95\%}} = 2.2 \pm 0.8 \mu\text{s}$. It will be seen in Sec. III B that these are small bubbles that exhibit a second harmonic resonance pattern.

A typical bubble of resonant size emits a high amplitude signal with an increased fundamental component of scatter (fundamental to harmonic ratio has been measured up to 4), and shows an increasing amplitude of scatter with time, as shown in the envelopes of RF signals in Figs. 2(c) and 2(d). In response to 550 kPa, bubbles of RMS fundamental scatter greater than 8 Pa, i.e., resonant bubbles, all have $\Delta t_{95\%} > 2.0 \mu\text{s}$, with a mean value $\overline{\Delta t_{95\%}} = 3.4 \pm 0.5 \mu\text{s}$; the latter value corresponds to the total pulse duration and is a manifestation of the clipping effect due to the short pulse duration. The same maximum value of $\Delta t_{95\%}$, $\Delta t_{95\%} = 3.8 \mu\text{s}$, occurs at the smallest value of resonant scatter, fundamental RMS $\approx 8 \text{ Pa}$, but also for a much larger value of fundamental RMS $\approx 20 \text{ Pa}$.

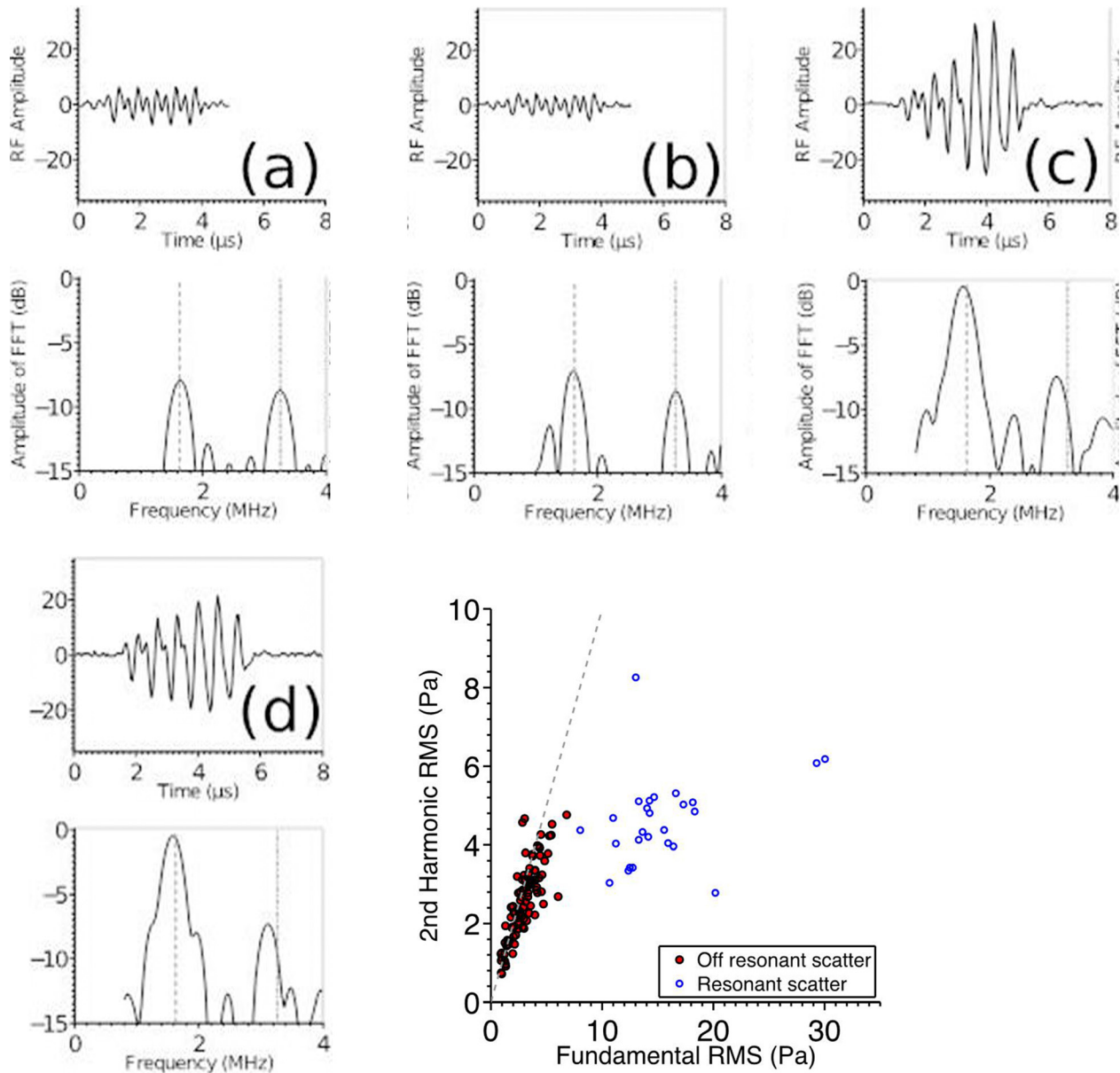


FIG. 2. (Color online) Definity[®] (Lantheus Medical Imaging, N. Billerica, MA) single microbubble acoustic signals in response to a six cycle 1.6 Hz 550 kPa incident pulse. Signals from bubbles below resonance (a),(b) and bubbles at and above resonance (c),(d) are shown, with a clear difference in both amplitude and envelope of response. Radio frequency (RF) signals are shown (top) with the amplitude of FFT shown below, normalized to peak scatter measured. Fundamental and second harmonic frequencies of transmit are indicated with grey dashed lines, showing a decreased frequency of scatter in both in the resonance bubbles, with a larger shift at the second harmonic value. RMS components of fundamental and second harmonic scatter are displayed in scatter graph (e), showing increased fundamental scatter in resonant bubbles. Equal fundamental and second harmonic is shown with a grey dashed line.

Figure 3 shows the variation of $\Delta t_{95\%}$ with incident acoustic pressure [Fig. 3(a) 187 kPa, Fig. 3(b) 275 kPa, Fig. 3(c) 375 kPa, Fig. 3(d) 550 kPa], illustrating this resonance characteristic. In response to each increasing acoustic pressure two distinct maxima occur at the maximum value $\Delta t_{95\%} \approx 3.8 \mu\text{s}$; the first one takes place at the onset of resonant acoustic signal and the second for a larger value of fundamental RMS. In fact, as the sound amplitude increases the second one provides the absolute maximum in time delay $\Delta t_{95\%}$. This is attributed to resonant and larger than resonant bubbles that exhibit fundamental and subharmonic resonance, respectively, and results in the widening of the resonant envelope in the time delay vs fundamental scatter plots. The increasing envelope of scatter at increased amplitudes has previously been identified as a

characteristic of forced damped harmonic oscillators driven at resonance. It is suggested here that as the sound amplitude increases a progressively larger number of bubbles enters the envelope of resonant scatter signifying the reduction in resonant frequency with increasing amplitude and the widening of the resonant spectrum that contains the fundamental and subharmonic resonances. A more detailed discussion illustrating this issue follows in Sec. III B, theory and simulation.

B. Theoretical analysis and simulations

Figure 4 shows example radial oscillations as predicted by the model proposed by Tsiglifs and Pelekasis (2008), which incorporates a MR shell model, for below resonance,

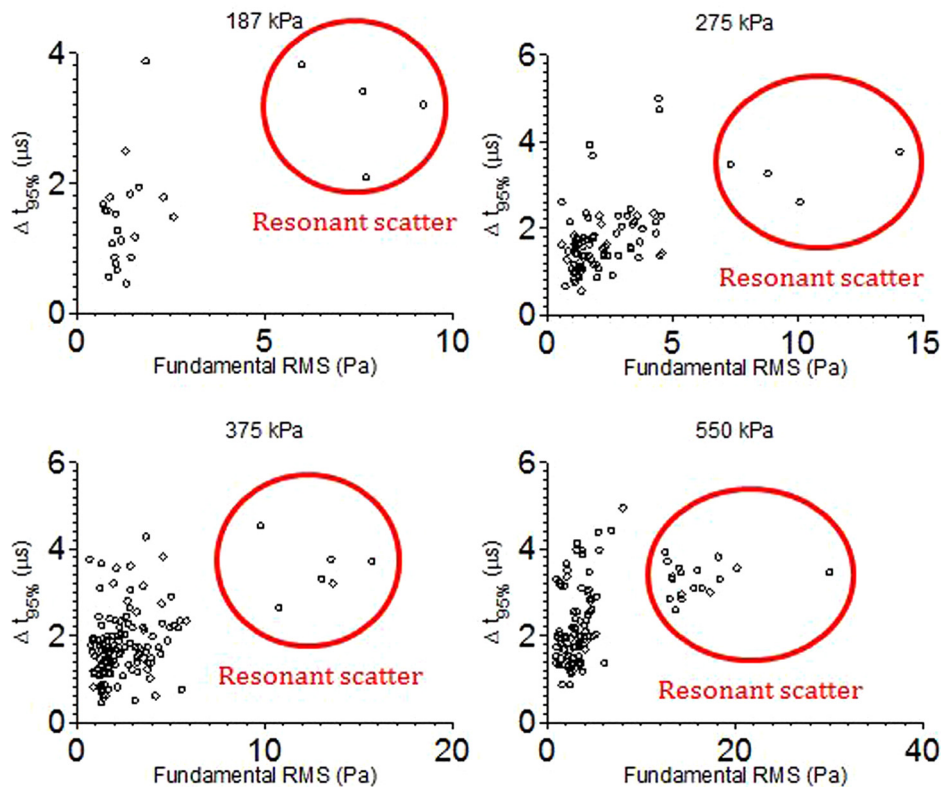


FIG. 3. (Color online) Time for the initial transient microbubble response taken to reach a value of 95% of peak scatter ($\Delta t_{95\%}$) plotted against fundamental RMS scatter (Pa) for increasing incident acoustic pressures, (a) 187 kPa, (b) 275 kPa, (c) 375 kPa, (d) 550 kPa.

resonant, and above resonance sizes, and the same shell viscoelastic parameters as in Fig. 1. The incident acoustic pulse was the same as for the experimental signals shown in Fig. 2, i.e., a rectangular pulse with a duration of six cycles at 1.6 MHz ($\Delta t \sim 4 \mu\text{s}$) amplitude set to 550 kPa and varying rest radius. The simulated radial oscillations shown in Figs. 4(a)–4(d) show similar characteristics as those measured experimentally [Figs. 2(a)–2(d)]. The simulations were repeated for a pulse duration of 20 cycles [Figs. 4(e)–4(h)] in order to illustrate the transient nature in the responses captured for 6 cycles [Figs. 4(a)–4(d)] without, however, exhibiting any significant compromise in the resonant behavior of the pulsating microbubbles. Furthermore, Figs. 4(i)–4(p) provide the FFT spectra of the simulated RMS scattered pressure signals illustrating similar deviations between primary and off-primary resonant scatter with the measured values [Figs. 2(a)–2(d)] while revealing the importance of subharmonic resonance, especially for large bubbles. No significant deviations are registered in the response to a 6 and 20 cycle pulse, besides the onset of steady pulsations beyond a certain time interval.

For bubbles below the resonance radius with $R_0 \sim 2.8 \mu\text{m}$, radial time series are provided in Figs. 4(a) and 4(e) in response to 6 and 20 cycle pulses, the MR model predicts a highly harmonic scattered pressure signal that is dominated by the second harmonic component [Figs. 4(i) and 4(m)] with constant amplitude across the six cycle response that is quite similar to the transmitted pulse. The time taken for the signal to grow to 95% of maximum scatter occurs within the first cycle of response, and it is approximately $\Delta t_{95\%} = 1 \mu\text{s}$ and followed by the onset of steady pulsations. As the bubble's radius is increased toward the primary resonance radius, radial time series at $R_0 \sim 3.5 \mu\text{m}$ and $5.3 \mu\text{m}$ are provided in Figs.

4(b), 4(c), 4(f), and 4(g) in response to a 6 and 20 cycle pulse, respectively, both the amplitude of oscillation and energy of acoustic scatter increase sharply, and the oscillation becomes dominated by the fundamental driving frequency [Figs. 4(j), 4(k), 4(n), and 4(o)]. The envelope of the oscillation is evident across the 6 and 20 cycle responses due to the large sound amplitude transfer of energy between the natural oscillation and emerging harmonics being intensified, especially the second harmonic and subharmonic components, and the time required for steady pulsation to take place increases; see Figs. 4(b), 4(c), 4(d), 4(f), 4(g), and 4(h) pertaining to equilibrium radii $R_0 = 3.5, 5.3,$ and $7.5 \mu\text{m}$ and $\varepsilon = 5.5$. When the bubble radius is relatively small, i.e., $R_0 = 3.5 \mu\text{m}$, the peak scatter occurs at the end of the third cycle of the response and the scattered pressure contains a significant second harmonic component [Figs. 4(j) and 4(n)], both in the transient and steady phases of the pulsation. As the bubble size further increases it reaches the realm of subharmonic resonance, $R_0 = 5.3$ and $7.5 \mu\text{m}$, and its response is characterized by an increasing subharmonic component of the scattered pressure [Figs. 4(k), 4(l), 4(o), and 4(p)] that maximizes the value of $\Delta t_{95\%}$.

Figure 5 is an attempt to reproduce the dynamic response from a bubble population captured by acoustic measurements in the manner depicted in Figs. 2(e) and 3(a)–3(d). Since the exact parameters of the population are not known we assume a uniform size distribution ranging from 2 to $8 \mu\text{m}$, and calculate the RMS components of the scattered pressure for a microbubble with rest radius in the above range. The results are then plotted so that each point corresponds to values obtained for a certain rest radius with each value carrying the same weight over the total population. In this fashion the relative importance of fundamental, second harmonic, and subharmonic scatter is illustrated for

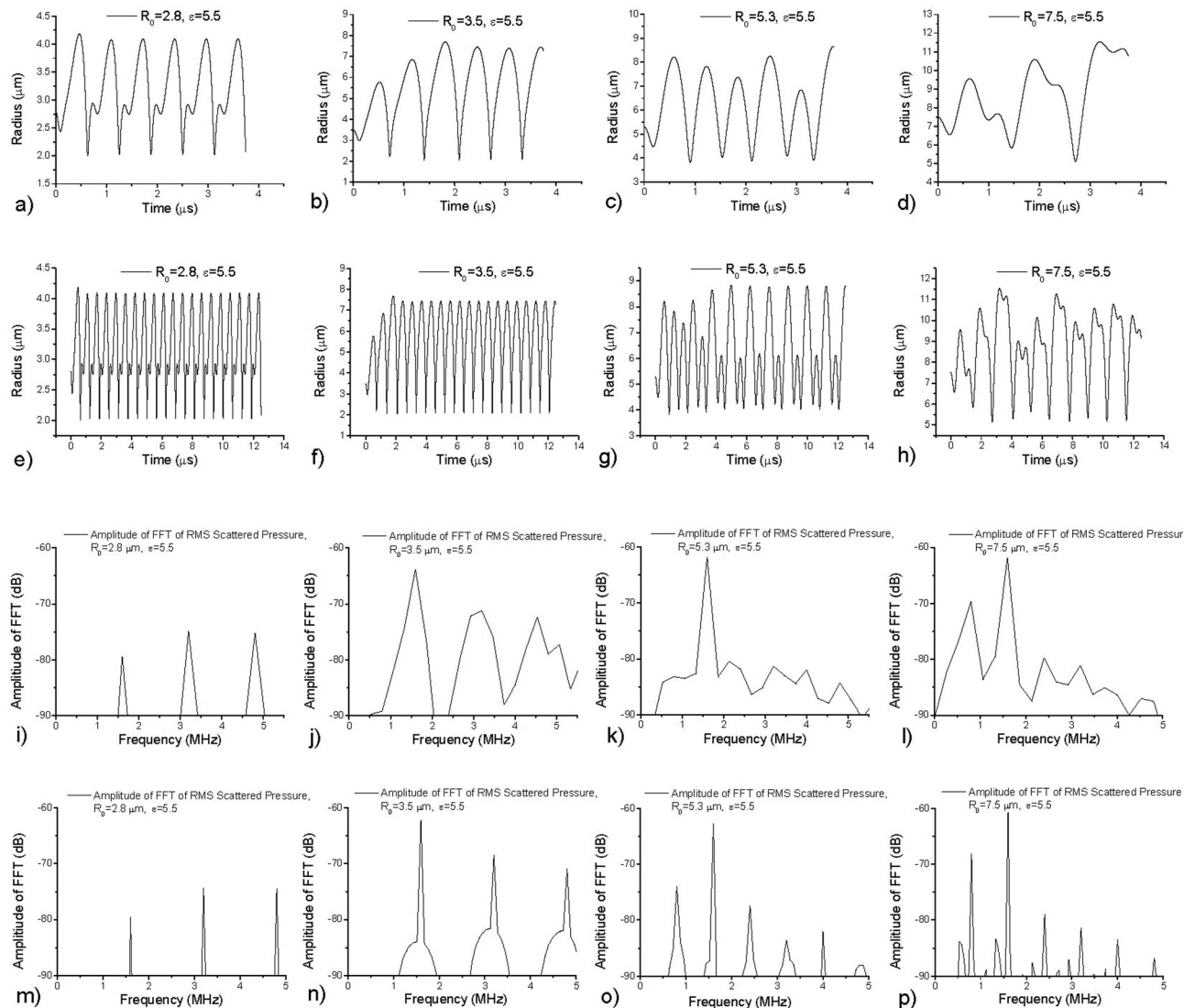


FIG. 4. Numerically obtained radial time series in response to a sinusoidal disturbance of rectangular shape with frequency 1.6 MHz and amplitude 550 kPa that lasts over 6 cycles, graphs (a)–(d), and over 20 cycles until steady pulsation has been achieved, graphs (e)–(h). The MR shell model is employed (Tsigliffis and Pelekasis, 2008) with shell parameters $\chi_s = 2.25 \text{ N/m}$, and $\mu_s = 1 \text{ Pa s}$. Graphs (i)–(l) and (m)–(p) provide the FFT decomposition of the RMS scattered pressure for the cases shown in (a)–(h).

MR [Figs. 5(a)–5(f)], and Hookean shells [Figs. 5(g)–5(l)], as well as the manner in which the corresponding resonances are manifested in the graph portraying the variation of the time delay to 95% scatter, $\Delta t_{95\%}$, as the amplitude increases. The graphs are arranged as a function of the fundamental component of the RMS scattered pressure with the first 3 pertaining to a 6 cycle pulse, followed by 3 similar graphs obtained for a longer 20 cycle pulse, in which case the microbubbles have enough available time to reach steady pulsation.

It should be stressed that, despite the transient nature of the dynamics in Figs. 5(a), 5(b), and 5(c), in comparison with the response to a longer pulse shown in Figs. 5(d), 5(e), and 5(f), respectively, the essential features of the response are captured, namely, the onset of first, second harmonic, and subharmonic resonance, which are intensified as the amplitude increases. This is most distinctly manifested in the time delay graphs [Figs. 5(c) and 5(f)], which both contain three distinct maxima obtained for relatively small, intermediate, and large values of the

fundamental component. These peaks are evident in the variation of the second harmonic and subharmonic components, but they are not as pronounced, especially the one corresponding to the second harmonic. In particular, as the sound amplitude increases the peaks in first and subharmonic scatter exhibit a gradually intensified deviation from the second harmonic resonance, which is weaker and appears for a much smaller fundamental RMS component. In the latter range of fundamental RMS the scattered signal contains a significant second harmonic component, which is followed by the resonant envelope mentioned above determined by the two resonant peaks pertaining to the fundamental and subharmonic components, as the fundamental RMS signal increases. A similar response pattern is identified in the second harmonic signal and time delay variations vs the fundamental component obtained in the acoustic measurements reported in Figs. 2 and 3.

In the following it will be seen that the above resonances are associated with the rest radii that are below resonant

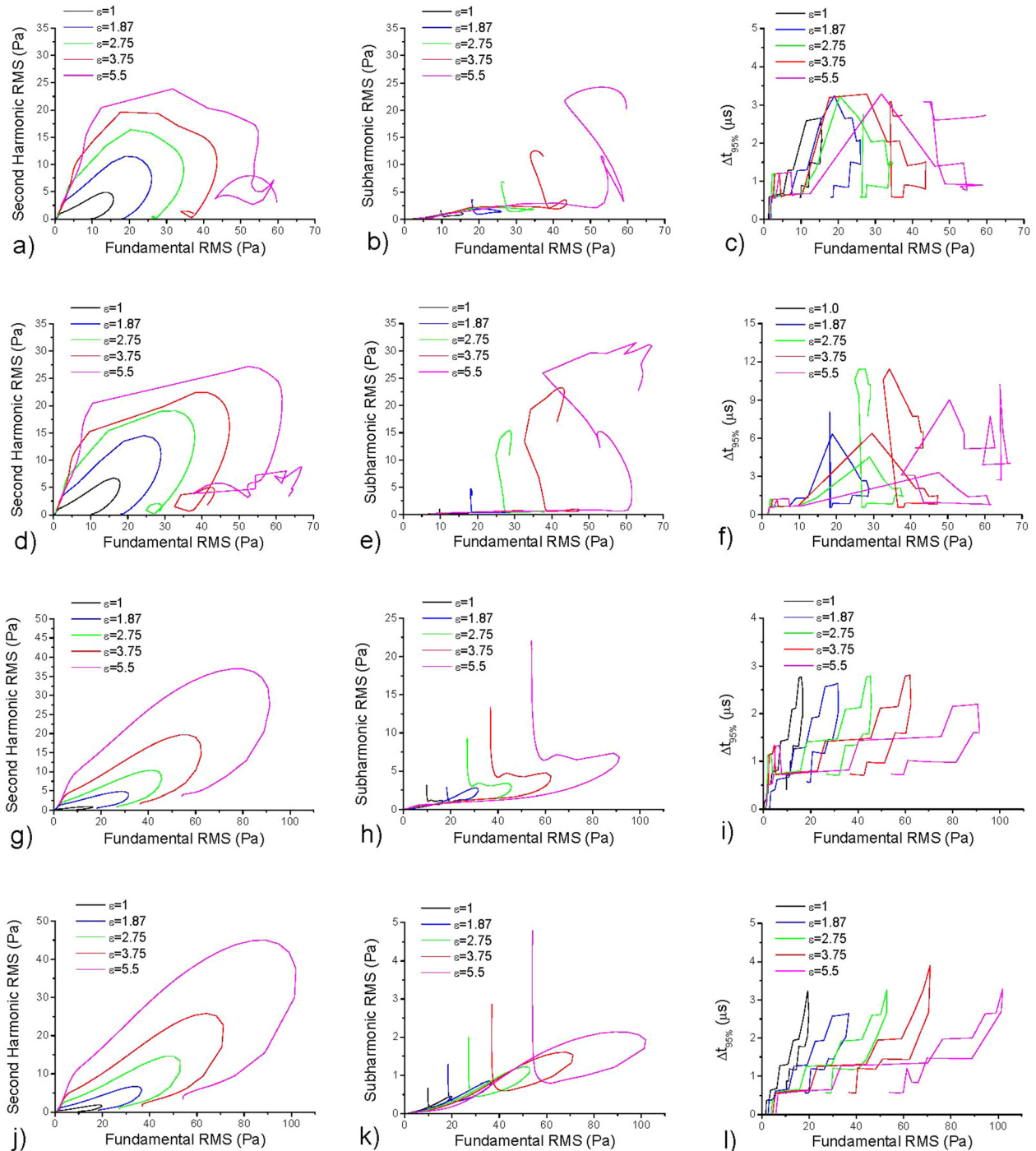


FIG. 5. (Color online) Variation of second harmonic and subharmonic components of the scattered pressure, at $r = 7.5$ cm, and the time delay to maximum scatter $\Delta t_{95\%}$ with the RMS of the fundamental component of the scattered pressure as the sound amplitude increases, subject to a 6 cycle, panels (a)–(c), and 20 cycle pulse, panels (d)–(f). The coating of the bubble is treated as a MR shell in panels (a)–(f), whereas panels (g)–(l) illustrate the same effects for a Hookean shell. The rest of the parameters are the same as those used in Figs. 1, 4, and 5.

for the second harmonic and above resonant for the subharmonic resonance (Figs. 6 and 7), and we will henceforth refer to this effect as the broadening of the resonant envelope. This pattern is more clearly registered in the response to the 20 cycle pulse [Fig. 5(f)] where during the phase of steady pulsation the fundamental and subharmonic components are intensified at resonant conditions. It should also be noted that due to the transient effects parameter $\Delta t_{95\%}$ is almost invariably equal to the pulse duration, $\Delta t \sim 3.5 \mu\text{s}$, in Fig. 5(c) for large amplitudes. This is resolved in Fig. 5(f)

where a longer pulse is applied. Nevertheless, $\Delta t_{95\%}$ is still controlled by the abovementioned resonances as can be surmised by cross-examining Figs. 5(a), 5(b), and 5(c) with Figs. 5(d), 5(e), and 5(f), respectively.

Simulated signals for Hookean shells that are characterized by a linear constitutive law (Tsigliffis and Pelekasis, 2008) are also provided in Figs. 5(g)–5(i) and Figs. 5(j)–5(l), for a 6 and a 20 cycle pulse, respectively, illustrating the absence of such a tendency in the variation of the second harmonic and subharmonic components and the time delay,

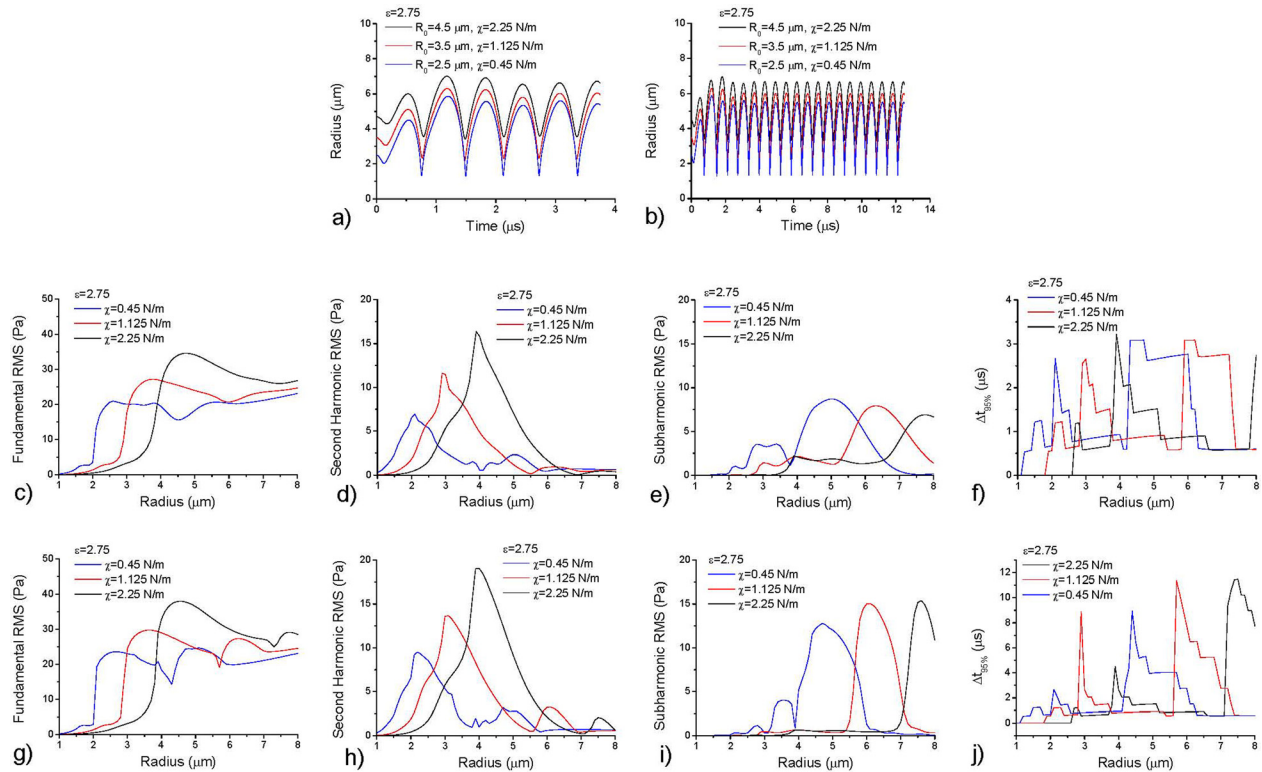


FIG. 6. (Color online) Microbubble responses approaching resonance with different area dilatation moduli, $\chi = 2.25, 1.125$, and 0.45 N/m. Radial time series, fundamental, second harmonic and subharmonic RMS pressures, as well as variation in time to 95% of peak scatter ($\Delta t_{95\%}$), are plotted against equilibrium radius as obtained for 6 cycle, panels (a) and (c)–(f), and 20 cycle pulses, panels (b) and (g)–(j).

$\Delta t_{95\%}$, to maximum scatter of the scattered signal from such bubbles. The scattered echoes and time delay graphs exhibit a linear part as a function of the fundamental component followed by a single common peak, with the acoustic emission from bubbles at resonance dominated by the fundamental frequency [Figs. 5(g)–5(l)].

Figure 6 focuses on the variation in the time to peak oscillation $\Delta t_{95\%}$ at resonance for decreasing shell stiffness, $\chi_s = 2.25, 1.125$, and 0.45 N/m, and its correlation with the resonant characteristics of the pulsating microbubble, in an effort to interpret the response pattern obtained via the

simulations shown in Fig. 5 and the acoustic measurements in Figs. 2 and 3. Bubbles of different radii and shell stiffness have been simulated. The latter parameter is varied in an effort to improve the agreement between experiments and simulations in terms of the fundamental RMS and obtain more reliable estimates of the area dilatation modulus of the shell. Figures 6(a) and 6(b) provide the radial time series at the respective resonant sizes that are seen to increase with increasing area dilatation χ , as expected based on linear analysis (Tsigliferis and Pelekasis, 2008). The response to a longer pulse is shown in Fig. 6(b) with the same effect on the radial

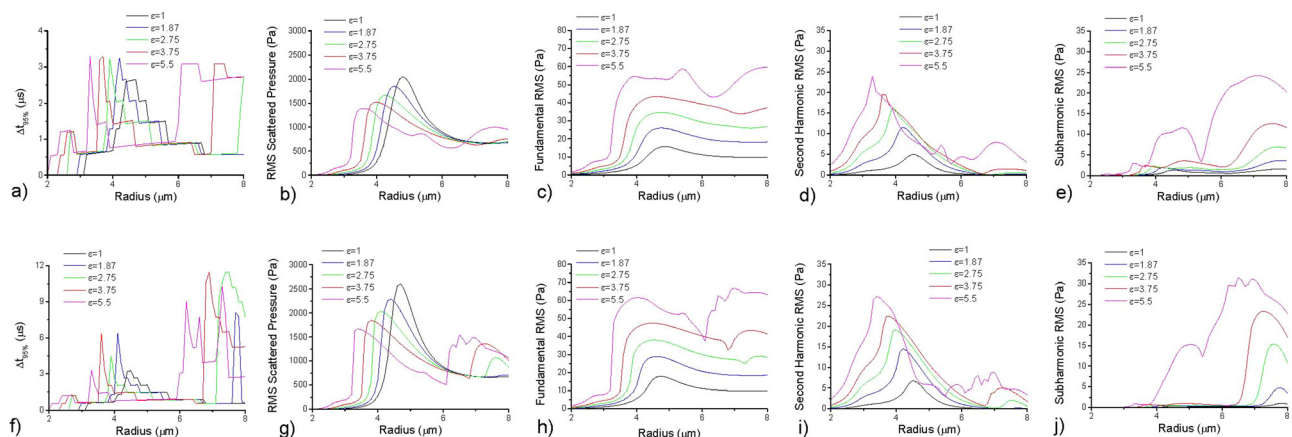


FIG. 7. (Color online) Variation of the time to peak scatter, $\Delta t_{95\%}$, RMS scattered pressure, and RMS of the fundamental, second harmonic, and subharmonic components of the scattered pressure, with initial microbubble radius R_0 as the incident acoustic pressure increases from 100 kPa to 550 kPa. Panels (a)–(e) and (f)–(j) portray the response subject to a 6 and a 20 cycle pulse, respectively, for a MR shell; the area dilatation is set to $\chi = 2.25$ N/m, while the RMS pressure has been calculated at a radial distance of 7.5 cm from the bubble center.

time series, indicating the onset of steady pulsation. This behavior is also reflected in the time to maximum oscillation $\Delta t_{95\%}$ plotted in Fig. 6(f), which reaches a local maximum for an increased resonant size as the shell area dilatation increases. In fact, upon comparing Fig. 6(f) against Figs. 6(c)–6(e) depicting a similar variation of fundamental, second harmonic, and subharmonic RMS pressure with the rest radius, it becomes clear that the peaks in time to maximum oscillation $\Delta t_{95\%}$ coincide with the bubble sizes that produce maximum response in the scattered pressure with respect to the second harmonic, fundamental, and subharmonic components. Since this is a second-order nonlinear effect it takes longer to evolve, and this also reflects in the resonant envelope exhibited by the radial time series pertaining to the resonant sizes in Fig. 6(a). This resonant behavior for bubbles with an elastic coating has also been reported elsewhere (Church, 1995), and it is interesting to note that it correlates well with the time to maximum scatter, even in the presence of transients. In particular, for each value of shell stiffness parameter a plateau in $\Delta t_{95\%}$ is reached around resonance at $\Delta t_{95\%} = 4.0 \mu\text{s}$. A maximum threshold in the time to peak oscillation is spread across a range of bubble radii, ΔR_0 , which is approximately $\Delta R_0 = 0.25 \mu\text{m}$ for each value of χ . Furthermore, at resonance the transient decay times, or time to maximum response, are of similar duration to the length of the six cycle incident pulse ($\Delta t_{95\%} \sim 4.0 \mu\text{s}$), indicating a clipping effect that characterizes transient behavior. Finally, it should be stressed that upon reducing the area dilatation modulus it is observed that the fundamental RMS pressure at resonance decreases, thus, approaching the experimentally observed values while corroborating the conjecture that the interrogated shells are quite soft, i.e., setting χ to 0.45 N/m provided the closest approximation to the experimental acoustic signals among the different values that were tested. This effort was not pursued further in the context of the present study since parameter estimation was not our primary concern.

The results of the simulations for longer pulses are plotted in Figs. 6(b), 6(g), 6(h), 6(i), and 6(j), confirming the relevance of transient signals in identifying resonance, as well as the clipping effect of shorter pulse durations. In particular, Fig. 6(b) shows the radial response from microbubbles with resonant equilibrium radius corresponding to the same stiffness parameters as in Fig. 6(a). It illustrates duration of transient through the time taken to reach maximum amplitude of radial excursion when the incident pulse is 20 or more cycles long, or $\geq 12 \mu\text{s}$ in duration. In each case, the transient response can clearly be seen to decay, and bubbles reach steady state response. Resonance radius is increased accordingly, from $R_{\text{res}} = 2.5 \mu\text{m}$ to $R_{\text{res}} = 3.5 \mu\text{m}$ and $4.5 \mu\text{m}$ as χ increases based on the fundamental response [Figs. 6(c) and 6(g)]. Figure 6(j) shows the effect of shell stiffness on the duration of transient decay at resonance, with a stiffer shell leading to the same increased resonant size obtained in Fig. 6(f) for a shorter pulse duration. An interesting aspect of the response pattern portrayed in Fig. 6 is that indeed the time delay to maximum scatter exhibits maxima that correspond to the three major resonances, i.e., second harmonic primary and subharmonic resonances, but the actual resonant size is

better correlated with the ones for which peaks are obtained in the subharmonic signal. This can be verified by cross-inspection of Figs. 6(c)–6(f) and 6(g)–6(j) where the alignment of the rest radii values that provide the peaks in time delay and subharmonic signal can be verified. This is a result of the longer time scale of the subharmonic signal, $\omega = \omega_f/2$, that reflects in the time required for the amplitude modulation to take place between the fundamental and the subharmonic components. Furthermore, the disparate resonant sizes pertaining to the second harmonic and subharmonic resonances is attributed to the inverse proportionality of resonance frequency of coated bubbles with respect to their sizes (Church, 1995; Tsigliferis and Pelekasis, 2008); see Eq. (2). Consequently, subharmonic resonance occurs at half the forcing frequency and requires a larger rest radius than the primary resonance.

As was mentioned above, the simulations indicate a marked difference as the sound amplitude varies, mainly as a result of the onset of the three major resonances. The latter effect becomes evident upon careful examination of the panels in Fig. 7 showing the variation of time to peak amplitude, scattered RMS pressure, and its fundamental, second harmonic, and subharmonic components plotted against the microbubble radius for increasing sound amplitude. In all cases a shift toward smaller sizes is detected at resonance, manifested in the reduction of the rest radii producing the dominant peaks in the scattered RMS pressure and time to peak amplitude as the sound amplitude increases. Repeating the simulations in response to a longer pulse duration, i.e., with a 20 cycle pulse, recovers the above behavior without significant discrepancies except for the more accurate calculation of the maximum time delay pertaining to the second, primary, and subharmonic resonant peaks as the sound amplitude increases, without however altering the rest radii for which these peaks occur. This kind of nonlinear behavior at resonance has been reported by Tsigliferis and Pelekasis (2008), and was mainly attributed to the strain softening nature of the shell material that becomes more evident with nonlinearity. In the latter study the same pattern of nonlinearity assumed the form of a reduction in resonance frequency with increasing sound amplitude for fixed equilibrium radius. Since the reduced resonance frequency is a sign of increased effective inertia of the microbubble with nonlinearity, one can interpret the reduction in resonant size with nonlinearity, for fixed frequency, as the tendency of the microbubble to establish the same amount of effective inertia in the face of nonlinearity by reducing its size. The same kind of second-order nonlinear effect has been predicted and observed previously by Morgan *et al.* (2000) and was attributed to the phase shift upon approaching resonance. The same phase shift during resonance is also responsible for the delay in achieving maximum signal, as illustrated by the sudden peaks in $\Delta t_{95\%}$ in Figs. 5(c), 5(f), 7(a), and 7(f) for sizes that coincide with the sizes required for resonance to take place [Figs. 7(b)–7(e) and 7(g)–7(j)].

As a result of the reduction in resonant size with increasing amplitude, the part of the bubble population that is in resonance increases, thus enhancing contrast in the scattered signal, especially as the subharmonic component is

intensified. In particular, for large amplitudes, e.g., $\varepsilon \geq 2.75$, the bubble acoustic response exhibits a two population pattern that largely consists of the weaker second harmonic resonance, which is characterized by below resonance sizes and dominates the initial linear part of the time delay vs fundamental RMS component plot, and the primary and subharmonic resonances. The latter two resonances occur for significantly larger values of the fundamental RMS component and generate an extended resonance envelope within which most of the scattered signal is obtained (Figs. 5 and 7). The bubble population with a registered signal within this envelope increases with increasing amplitude since, for a fixed bubble size distribution, the resonant size decreases with nonlinearity; see also Fig. 7. Furthermore, the signals from the bubble populations corresponding to the second harmonic resonance and the primary and subharmonic resonance are becoming quite distinct with nonlinearity due to the significantly larger fundamental signal emitted by the latter two. This feature is also evident in the experimental results presented in Figs. 2(e) and 3, it is associated with the resonant behavior of MR microbubbles, and can be employed for controlling and optimizing the signal from such bubble populations.

This pattern is in marked distinction with the behavior exhibited by the Hookean shells for which the fundamental resonance determines the acoustic response. It is also important to note at this point that for Hookean shells the simulations reveal a distinct tendency for a nonlinear shift toward larger bubbles at resonance [Fig. 8] for the fundamental, second harmonic, and subharmonic components. In contrast to MR shells, for microbubbles with neo-Hookean-type coating this reflects a shift to larger frequencies at resonance as nonlinearity is intensified, when their size is fixed. Similarly, the time delay to maximum scatter only provides one peak corresponding to primary resonance. The emitted sound signal consists of two almost linear regimes, corresponding to below and above resonant bubble sizes, respectively, that enclose a narrow regime of resonant scatter [Figs. 5(g)–5(l)].

IV. CONCLUSIONS

The impact of transient effects on acoustic signals from pulsating microbubbles for relatively short pulses (six cycles at 1.6 MHz) is shown to emerge in the context of harmonic resonance as the sound amplitude increases. This is a result of the amplitude modulation reflecting energy transfer between the forcing and natural pulsations at resonant conditions (see also Figs. 1, 2, and 4), but also between the forcing and second harmonic and subharmonic components at large sound amplitudes. Consequently, there is a time delay in the system's effort to achieve peak amplitude during steady pulsation, which is registered as parameter $\Delta t_{95\%}$. It was systematically seen in the context of the present study that the time to peak amplitude $\Delta t_{95\%}$ is a reliable marker of resonance. It assumes a local maximum for bubble sizes pertaining to the primary, second harmonic, and subharmonic resonances (Figs. 6 and 7), and this effect is accentuated for short pulse durations. This behavior was illustrated in the experimental data presented herein and verified by the simulations that were performed, which recovered the above maxima of parameter $\Delta t_{95\%}$ in its graph against the fundamental RMS pressure (Figs. 5 and 9).

The rich harmonic content manifested in the experimental measurements depicted and recovered by the simulations is a result of the strain softening nature of the lipid monolayer shells (Tsirlifis and Pelekasis, 2008). An additional important feature of strain softening shell behavior is the discrepancy in resonant radius between the fundamental, second harmonic, and subharmonic acoustic components with increasing sound amplitude. Thus, a smaller and a larger resonant size are obtained in addition to the fundamental one, which induce the appearance of a second harmonic and a subharmonic resonant regime in the acoustic signal, respectively. As a result of the reduction in the above resonant sizes with increasing sound amplitude, in order to accommodate the additional inertia generated by nonlinearity for such microbubbles, an increasingly larger number of bubbles scatter sound in this regime of high harmonic content as the

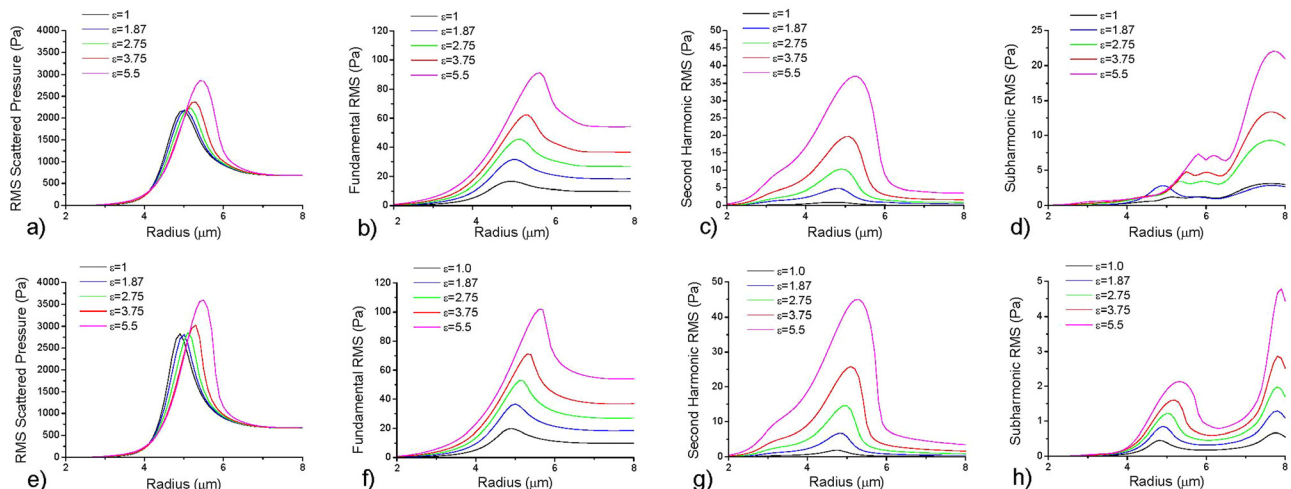


FIG. 8. (Color online) Variation of the RMS scattered pressure and RMS of the fundamental, second harmonic, and subharmonic components of the scattered pressure, with initial microbubble radius R_0 as the incident acoustic pressure increases from 100 kPa to 550 kPa. Panels (a)–(d) and (e)–(h) portray the response subject to a 6 and a 20 cycle pulse, respectively, for a Hookean shell; the area dilatation is set to $\chi = 2.25$ N/m and the RMS pressure has been calculated at a radial distance of 7.5 cm from the bubble center.

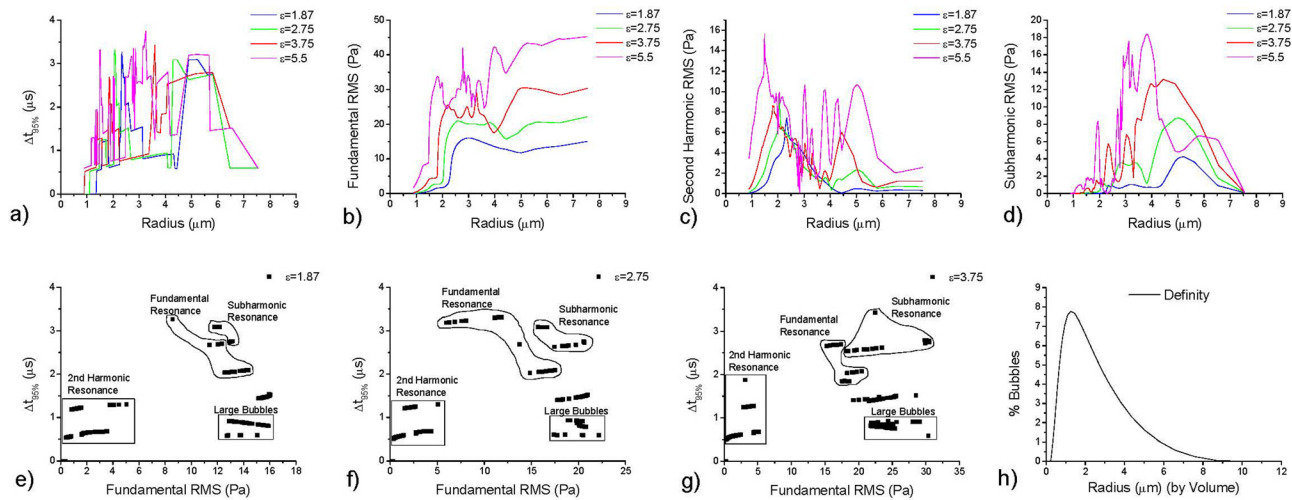


FIG. 9. (Color online) Simulated variation of the time to peak scatter, $\Delta t_{95\%}$, and RMS of the fundamental, second harmonic, and subharmonic components of the scattered pressure with initial microbubble radius R_0 , panels (a)–(d) respectively, as the incident acoustic pressure increases, for a MR shell with area dilatation modulus $\chi = 0.45$ N/m that is subject to a six cycle pulse. Panels (e)–(g), portray the time to peak scatter, $\Delta t_{95\%}$, as a function of fundamental scatter with increasing sound amplitude, calculated based on a realistic microbubble size distribution, panel (h).

sound amplitude increases. Furthermore, a two population pattern emerges in the emitted acoustic signal corresponding to (a) less than resonant size bubbles, i.e., the linear part of the second harmonic or time delay vs first fundamental plot that contains the peak due to second harmonic resonance, and (b) resonant and larger than resonant size bubbles, occupying the resonant envelope determined by the fundamental and subharmonic resonant peaks. Figure 9 illustrates the above pattern in the response of a bubble population with a size distribution [Fig. 9(h)] that is based on the one employed in the experimental measurements shown in Figs. 2 and 3. The bubble cluster that is identified in Figs. 9(e)–9(g) as large bubbles corresponds to microbubbles with rest radii $R_0 \geq 6 \mu\text{m}$. They are conjectured to break up during insonation at large sound amplitudes, hence they do not register an acoustic signal in the measurements presented in Fig. 3. Furthermore, the area dilatation modulus χ is set to 0.45 N/m in the simulations shown in Fig. 9, corresponding to a soft shell, in an effort to recover the fundamental RMS in the scattered pressure as accurately as possible, given the complexity of the problem. Such an agreement is not possible with the linear Hookean shells, which do not possess the rich harmonic content of MR shells. They are characterized by an increase in resonant size with nonlinearity (Fig. 8), and hence do not provide the wide resonant envelope in the time decay vs fundamental RMS pressure plots.

Signal processing, using microbubble exposure to a number of pulses, enables both tissue scatter cancellation and exploitation of the microbubble nonlinear properties. While the former has proved successful, the latter is difficult to assess due to a lack of understanding of the physical behavior of coated microbubbles. The response pattern examined herein is an important aspect of the dynamic response of lipid shells that can be used to identify the nature of such microbubbles in acoustic measurements and provide optimal signal processing protocols by exploiting bubble sizes with favorable second harmonic or, preferably, subharmonic to fundamental harmonic ratio during resonance.

ACKNOWLEDGMENTS

N.P. and K.E. wish to acknowledge financial support by the European Union (European Social Fund, ESF) and Greek national funds through the Operational Program “Education and Lifelong Learning” of the National Strategic Reference Framework (NSRF) via Research Funding Programs Aristeia I and Heraclitus II—Investing in knowledge society through the European Social Fund.

- Bouakaz, A., Versluis, M., and de Jong, N. (2005). “High-speed optical observations of contrast agent destruction,” *Ultrasound Med. Biol.* **31**(3), 391–399.
- Cheung, K., Couture, O., Bevan, P. D., Burns, P. N., and Foster, F. S., (2005). “The effect of bubble size distribution and driving frequency on the ‘subharmonic’ response from Definity microbubbles,” in *2005 IEEE Ultrasonics Symposium*.
- Chin, C. T., Lancée, C., Borsboom, J., Mastik, F., Frijlink, M. E., de Jong, N., Versluis, M., and Lohse, D. (2003). “Brandaris 128: A digital 25 million frames per second camera with 128 highly sensitive frames,” *Rev. Sci. Instrum.* **74**(12), 5026–5034.
- Chomas, E., Dayton, P., May, D., and Ferrara, K. (2001). “Threshold of fragmentation for ultrasonic contrast agents,” *J. Biomed. Opt.* **6**, 141–150.
- Christensen-Jeffries, K., Browning, R. J., Tang, M. X., Dunsby, C., and Eckersley, R. J. (2015). “*In vivo* acoustic super-resolution and super-resolved velocity mapping using microbubbles,” *IEEE Trans. Med. Imag.* **34**(2), 433–440.
- Church, C. C. (1995). “The effects of an elastic solid surface layer on the radial pulsations of gas bubbles,” *J. Acoust. Soc. Am.* **97**, 1510–1521.
- Dayton, P. A., Morgan, K. E., Klibanov, A. L., Brandenburger, G. H., and Ferrara, K. W. (1999). “Optical and acoustical observations of the effects of ultrasound on contrast agents,” *IEEE Trans. Ultrason. Ferroelectr. Freq. Control* **46**(1), 220–232.
- de Jong, N., Cornet, R., and Lancée, C. T. (1994a). “Higher harmonics of vibrating gas-filled microspheres. Part one: Simulations,” *Ultrasonics* **32**(6), 447–453.
- de Jong, N., Cornet, R., and Lancée, C. (1994b). “Higher harmonics of vibrating gas-filled microspheres, Part two: Measurements,” *Ultrasonics* **32**(6), 455–459.
- de Jong, N., Emmer, M., Chin, C. T., Bouakaz, A., Mastik, F., Lohse, D., and Versluis, M. (2007). “‘Compression-only’ behavior of phospholipid-coated contrast bubbles,” *Ultrasound Med. Biol.* **33**(4), 653–656.
- Dollet, B., van der Meer, S. M., Garbin, V., de Jong, N., Lohse, D., and Versluis, M. (2008). “Nonspherical oscillations of ultrasound contrast agent microbubbles,” *Ultrasound Med. Biol.* **34**, 1465–1473.
- Emmer, M., Vanwamel, A., Goertz, D., and de Jong, N. (2007). “The onset of microbubble vibration,” *Ultrasound Med. Biol.* **33**(6), 941–949.

- Errico, C., Osmanski, B. F., Pezet, S., Couture, O., Lenkei, Z., and Tanter, M. (2015). "Transcranial functional ultrasound imaging of the brain using microbubble-enhanced ultrasensitive Doppler," *Neuroimage* **124**(Pt A), 752–761.
- Feinstein S. B., Cheirif, J., Ten Cate, F. J., Silverman, P. R., Heidenreich, P. A., Dick, C., Desir, R. M., Armstrong, W. F., Quinones, M. A., and Shah P. M. (1990). "Safety and efficacy of a new transpulmonary ultrasound contrast agent: Initial multicenter clinical results," *J. Am. Coll. Cardiol.* **16**(2), 316–324.
- Ferrara, K., Pollard, R., and Borden, M. (2007). "Ultrasound microbubble contrast agents: Fundamentals and application to gene and drug delivery," *Annu. Rev. Biomed.* **9**, 415–447.
- Flynn, H. G., and Church, C. C. (1988). "Transient pulsations of small gas bubbles in water," *J. Acoust. Soc. Am.* **84**(3), 985–998.
- Frinking, P. J., and de Jong, N. (1998). "Acoustic modeling of shell-encapsulated gas bubbles," *Ultrasound Med. Biol.* **24**(4), 523–533.
- Goertz, D. E., de Jong, N., and van der Steen, A. F. V. (2007). "Attenuation and size distribution measurements of DefinitTM and manipulated DefinityTM populations," *Ultrasound Med. Biol.* **33**(9), 1376–1388.
- Hoff, L., Sontum, P. C., and Hoff, B. (1996). "Acoustic properties of shell-encapsulated, gas-filled ultrasound contrast agents," in *Proceedings of the 1996 IEEE Ultrasonics Symposium*, November 3, Vol. 2, pp. 1441–1444.
- Kaufmann, B. A., Wei, K., and Linder, J. R. (2007). "Contrast echocardiography," *Curr. Probl. Cardiol.* **32**(2), 51–96.
- Keller, J. B., and Miksis, M. (1980). "Bubble oscillations of large amplitude," *J. Acoust. Soc. Am.* **68**, 628–633.
- Khismatullin, D. B., and Nadim, A. (2002). "Radial oscillations of encapsulated microbubbles," *Phys. Fluids* **14**, 3534–3556.
- Leighton, T. G. (1989). "Transient excitation of insonated bubbles," *Ultrasonics* **27**(1), 50–53.
- Marmottant, P., van der Meer, S., Emmer, M., Versluis, M., de Jong, N., Hilgenfeldt, S., and Lohse, D. (2005). "A model for large amplitude oscillations of coated bubbles accounting for buckling and rupture," *J. Acoust. Soc. Am.* **118**(6), 3499–3505.
- Morgan, K. E., Allen, J. S., Dayton, P. A., Chomas, J. E., Klibanov, A. L., and Ferrara, K. W. (2000). "Experimental and theoretical evaluation of microbubble behavior: Effect of transmitted phase and bubble size," *IEEE Trans. Ultrason. Ferroelectr. Freq. Control* **47**(6), 1494–1509.
- Overvelde, M., Garbin, V., Sijl, J., Dollet, B., de Jong, N., Lohse, D., and Versluis, M. (2010). "Nonlinear shell behavior of phospholipid-coated microbubbles," *Ultrasound Med. Biol.* **36**(12), 2080–2092.
- Paul, S., Katiyar, A., Sarkar, K., Chatterjee, D., Shi, W. T., and Forsberg, F. (2010). "Material characterization of the encapsulation of an ultrasound contrast microbubble and its subharmonic response: Strain-softening interfacial elasticity model," *J. Acoust. Soc. Am.* **127**(6), 3846–3857.
- Postema, M., Bouakaz, A., Chin, C. T., and de Jong, N. (2003). "Simulations and measurements of optical images of insonified ultrasound contrast microbubbles," *IEEE Trans. Ultrason. Ferroelectr. Freq. Control* **50**(5), 523–536.
- Prosperetti, A., and Lezzi, A. (1986). "Bubble dynamics in a compressible liquid. Part 1. First-order theory," *J. Fluid Mech.* **168**(1), 457–478.
- Raymond, J. L., Luan, Y., van Rooij, T., Kooiman, K., Huang, S. L., McPherson, D. D., Versluis, M., de Jong, N., and Holland, C. K. (2015). "Impulse response method for characterization of echogenic liposomes," *J. Acoust. Soc. Am.* **137**(4), 1693–1703.
- Sboros, V. (2008). "Response of contrast agents to ultrasound," *Adv. Drug Deliv. Rev.* **60**, 1117–1136.
- Sboros, V., Moran, C. M., Pye, S. D., and McDicken, W. N. (2003). "The behaviour of individual contrast agent microbubbles," *Ultrasound Med. Biol.* **29**(5), 687–694.
- Sboros, V., Pye, S. D., Anderson, T. A., Moran, C. M., and McDicken, W. N. (2007). "Acoustic Rayleigh scattering at individual micron-sized bubbles," *Appl. Phys. Lett.* **90**(12), 123902.
- Sboros, V., Pye, S. D., MacDonald, C. A., Gomatam, J., Moran, C. M., and McDicken, W. N. (2005). "Absolute measurement of ultrasonic backscatter from single microbubbles," *Ultrasound Med. Biol.* **31**(8), 1063–1072.
- Shi, W. T., and Forsberg, F. (2000). "Ultrasonic characterization of the non-linear properties of contrast microbubbles," *Ultrasound Med. Biol.* **26**(1), 93–104.
- Sijl, J., Gaud, E., Frinking, P. J., Ardit, M., de Jong, N., Lohse, D., and Versluis, M. (2008). "Acoustic characterization of single ultrasound contrast agent microbubbles," *J. Acoust. Soc. Am.* **124**(6), 4091–4097.
- Sijl, J., Overvelde, M., Dollet, B., Garbin, V., de Jong, N., Lohse, D., and Versluis, M. (2011). "'Compression-only' behavior: A second-order non-linear response of ultrasound contrast agent microbubbles," *J. Acoust. Soc. Am.* **129**(4), 1729–1739.
- Stride, E., and Saffari, N. (2003). "On the destruction of microbubble ultrasound contrast agents," *Ultrasound Med. Biol.* **29**(4), 563–573.
- Strouthos, C., Lampaskis, M., Sboros, V., and McNeilly, A. (2010). "Indicator dilution models for the quantification of microvascular blood flow with bolus administration of ultrasound contrast agents," *IEEE Trans Ultrason Ferroelectr Freq Control* **57**(6), 1296–1310.
- Thomas, D. H., Butler, M. B., Anderson, T., Steel, R., Pye, S. D., Poland, M., Brock-Fisher, T., McDicken, W. N., and Sboros, V. (2009a). "Single microbubble response using pulse sequences: Initial results," *Ultrasound Med. Biol.* **35**(1), 112–119.
- Thomas, D. H., Looney, P., Steel, R., Pelekasis, N., McDicken, W. N., Anderson, T., and Sboros, V. (2009b). "Acoustic detection of microbubble resonance," *Appl. Phys. Lett.* **94**(24), 243902.
- Tsigliffis, K., and Pelekasis, N. A. (2008). "Nonlinear radial oscillations of encapsulated microbubbles subject to ultrasound: The effect of membrane constitutive law," *J. Acoust. Soc. Am.* **123**(6), 4059–4070.
- Tsigliffis, K., and Pelekasis, N. (2011). "Parametric stability and dynamic buckling of an encapsulated micro-bubble subject to acoustic disturbances," *Phys. Fluids* **23**, 012102.
- Tsigliffis, K., and Pelekasis, N. (2013). "Simulations of insonated contrast agents: Saturation and transient break-up," *Phys. Fluids* **25**, 032109.
- van der Meer, M., Dollet, B., Voormolen, M. M., Chin, C. T., Bouakaz, A., De Jong, N., Versluis, M., and Lohse, D. (2007). "Microbubble spectroscopy of ultrasound contrast agents," *J. Acoust. Soc. Am.* **121**(1), 648–656.